POLITECNICO DI TORINO
Repository ISTITUZIONALE

Proceedings of the Merck Young Chemists' Symposium 2019

Original
Proceedings of the Merck Young Chemists' Symposium 2019 / Annunziato, G.; Atzori, M.; Bella, F.; Bonfio, C.; Cinti, S.; Da Pian, M.; Lazazzara, V.; Lenci, E.; Paone, E.; Ponte, F.; Rivoira, L.; Schlich, M.; Triggiani, L.. - ELETTRONICO. - (2019), pp. 1-246.

Availability:
This version is available at: 11583/2803452 since: 2020-03-16T14:23:31Z

Publisher:
Società Chimica Italiana

Published
DOI:

Terms of use:

This article is made available under terms and conditions as specified in the corresponding bibliographic description in the repository

Publisher copyright

(Article begins on next page)

21 April 2026

75th International Astronautical Congress (IAC), Milan, Italy, 14-18 October 2024.
Copyright ©2024 by the International Astronautical Federation (IAF). All rights reserved.

IAC-24-A3.IP.146.x89090

Minimum-Propellant Optimal Trajectories for the De-Orbiting of Decommissioned Satellites in Lunar Polar Graveyard Regions

Alessandro Nitti[a]*, Luigi Mascolo[b], Manuela Battipede[c]

Dipartimento di Ingegneria Meccanica e Aerospaziale, Politecnico di Torino, 24 Corso Duca degli Abruzzi, 10129 Turin, Italy
[a] alessandronitti77@gmail.com, [b] luigi.mascolo@polito.it, [c] manuela.battipede@polito.it
* Corresponding Author

Abstract

NASA's ambitious plans for sustained human presence in cislunar space, e.g. the Lunar Orbital Platform-Gateway program, has raised interest in cislunar orbits, looking for some desirable properties such as relatively low transfer costs from Earth, low orbit maintenance costs, and favourable communications opportunities with both Earth and the lunar south pole. As the cislunar region is anticipated to become increasingly populated with spacecraft, including potential debris, it is important to highlight the necessity of strategic deorbiting planning and compliance with international laws governing space debris. This study focuses on optimizing lunar deorbiting trajectories that use electric propulsion and depart from a NRHO, with a particular emphasis on minimizing propellant usage. The chosen reference orbit is the Gateway's southern L2 NRHO, with perilune and apolune radii of 3,300 km and 70,000 km and 9:2 synodic resonance with respect to the Moon's orbit around Earth. The optimization is carried out by an indirect method based on the Optimal Control Theory that transforms the propellant minimization problem into a Two-Point Boundary Value Problem. The single-shooting method shows bang-bang control derived from the Pontryagin's Maximum Principle to optimize the trajectories, ensuring that a specific region in the lunar north pole is targeted. The dynamic model considers 3-body gravitation (spacecraft subject to Earth and Moon gravity) within the Circular Restricted Three-Body Problem. Results identify a specific orbital arc in the NRHO, post-apolune, which is deemed ideal for de-orbiting the satellite via a two-burn trajectory that enables direct disposal towards the lunar north pole, significantly reducing propellant consumption allowing the mission to allocate more fuel for earlier operational phases, effectively extending the mission's operational lifespan.

Keywords: Near-Rectilinear Halo Orbit · Indirect optimization · Deorbiting trajectories · Graveyard region · Circular estricted three-body problem

1. Introduction

In the evolving panorama of global space exploration, the Moon and cislunar space is increasingly capturing the interest of major space agencies and private companies worldwide. The cislunar domain, identified as that area of deep space under the gravitational influence of the Earth-Moon (EM) system, offers affordable near-term opportunities to help pave the way for future global human exploration acting as a crucial link between current missions and future deep space endeavors. The upcoming direction is to exploit Earth's orbital environment, the surface of the Moon, and cislunar space to foster the critical technologies, operational capabilities, and commercial space economy with a view to sustainable human presence on the Moon, Mars, and beyond.

In recent years, space mission design has focused on three-dimensional periodic and quasi-periodic orbits near the libration points in the Earth-Moon three-body problem. Consequently, over the past two decades, there has been a growing interest in the concept of establishing a manned facility in a long-term relatively stable orbit in lunar vicinity. Missions may be established in EM libration orbits as a part of communication or navigation architecture, like in the ESA's Moonlight initiative [1], or to deploy and service spacecraft either in transit from the Moon or stationed at other Sun-Earth or Earth-Moon libration regions.

The first mission to orbit the EM Lagrange points was the ARTEMIS (EML_1 and EML_2 Lissajous orbits, on either side of the Moon), part of the THEMIS extended mission of NASA with the aim of studying a type of magnetic phenomena called substorms in Earth's magnetosphere that tend to intensify auroras near Earth's poles [2, 3]. Then, the CNSA with its Chinese Lunar Exploration Program launched and will launch spacecraft towards libration point orbits like Chang'e 5-T1 and Queqiao relay satellite of Chang'e 4 mission respectively on a EML_2 Lissajous orbit and a EML_2 Halo orbit [4]. JAXA's EQUULEUS cubesat was launched in 2022 to reach a quasi-periodic Halo orbit around EML_2 using lunar flybys and solar perturbation in order to study the Earth's plasmasphere and demonstrate trajectory control techniques exploiting Sun-Earth-Moon dynamics [5].

Copyright ©2024 by the International Astronautical Federation (IAF). All rights reserved.

Among other initiatives and space programs, the Artemis one is the most ground-breaking. The main objective of NASA's missions, in collaboration with ESA, JAXA, DLR, ASI, ISA and CSA, is to land the first woman and first person of color on the Moon, explore the lunar surface more than ever before, and lay the groundwork for sending astronauts to Mars [6]. Hand in hand with Artemis program, NASA and its partners will assemble the Lunar Orbital Platform-Gateway in a designated NRHO, a lunar space station much smaller and more focused platform than the International Space Station, to serve as a hub for next Artemis missions. Gateway is a vital component of the NASA-led program to return to the Moon and pave the way for future Mars exploration. For long-term operations, the LOP-G acts as a staging area for both human and robotic lunar expeditions, extending the duration of stays on the Moon and potentially accommodating multiple surface visits within a single mission [7]. In the realm of numerous possibilities, the Gateway Program opted for a NRHO of the EML_2 southern family as its operational orbit with a 9:2 lunar synodic resonance.

This ambitious program will bring together a growing presence of commercial, civil, and military stakeholders in the cis-lunar space, with the potential to navigate to different orbits around the Moon. This will entail a carefully orchestrated sequence of multiple launches in lunar orbit and spacecraft dockings with the forthcoming LOP-G. However, alongside the promise of these advancements lies a considerable challenge that must be addressed: the potential creation of significant amounts of space debris. The increase in satellite launches and orbital activities raises concerns about the environmental impact on the space surrounding Earth and the Moon. Space debris, consisting of defunct satellites, discarded rocket stages and fragments from erosion and collisions, poses a serious threat to operational spacecraft, including crewed missions and essential satellite infrastructure, limiting the ability to launch new spacecraft and eventually making entire orbits unusable. Another consequence is an increase of costs for space operations by requiring efforts to shield against or maneuver around it.

To comply with current and future regulations and prevent the contamination of cislunar space, upcoming missions must minimize their debris production and carefully orchestrate the disposal of involved spacecraft. Given the intricate dynamic environment, the challenge of End-of-Life disposal becomes notable for cislunar missions. Drawing from existing research [8, 9] and the historical record of previous missions, a cislunar spacecraft at EOL has three primary disposal strategies: executing an Earth atmospheric re-entry [10], moving to a stable graveyard orbit (cislunar or heliocentric) or de-orbiting onto the lunar surface [11]. Each presents specific constraints, advantages and drawbacks. Earth re-entry is a well-established practice in Space Debris Mitigation for Earth-orbiting missions but is less common for lunar mission disposal due to the high transfer costs back to Earth and operational complexity. More cost-effective alternatives leverage the dynamics of the Sun-Earth-Moon system, harnessing the concept of graveyard orbit (often used for satellites on GEOs) but with many factors to deal with, given the complex dynamics. On the other hand, several missions have opted for lunar impact as a method of disposal [12, 13]. In this case impacts must be strategically managed to minimize risk to human assets and historical landmarks on the Moon taking into account the possibility of targeting a specific location used as graveyard in which the remnants of spacecraft intentionally deorbited on the surface could provide a rich source of raw materials more accessible and practical for future utilization.

The core of this study is the optimization of electric propulsion de-orbiting trajectories with a view towards utilizing lunar impact in a northern polar graveyard region as a disposal strategy, with a particular emphasis on minimizing propellant usage. This strategy is evaluated not just for its potential to mitigate space debris, but also for its prospective contribution to the lunar economy by recycling the materials from the impacted spacecraft. The orbit chosen as the departure orbit is the LOP-G's Southern EML_2 NRHO, anticipated to be the primary destination for spacecraft in the coming years and potentially the main source of artificial debris in cislunar space.

The optimization is carried out with an indirect method based on the Optimal Control Theory (OCT), which transforms the propellant minimization problem into a Two-Point Boundary Value Problem (TPBVP). Pontryagin's Maximum Principle (PMP) allows the definition of a bang-bang control to optimize the trajectories starting from various points on the NRHO, ensuring that a specific region at the lunar north pole is targeted maximizing the final mass and, equivalently, minimizing the propellant consumption.

2. Background

The purpose of this section is to introduce the dynamical model with its equations, the NRHO selected as departing orbit and provide the tools for the optimization problem.

2.1 Circular restricted three-body problem

A generic three-body problem (3BP) is related to a generic binary system composed of two primary bodies orbiting around its barycenter, both modeled as point-masses of value m_1 and m_2 for the bigger and smaller, respectively, which mutually influence the 3D motion of the third body (e.g. the spacraft). Under the assumption of negligible mass of the third body and circular motion of the two primaries around their common center of mass,

Copyright ©2024 by the International Astronautical Federation (IAF). All rights reserved.

the transition from 3BP to circular restricted three-body problem (CR3BP) is made. Essentially, the third body is influenced by both gravitational forces of the two primary bodies without influencing their relative motion. The spacecraft dynamics equations in non-dimensional form, considering low-thrust propulsion, are described by the following set of ordinary differential equations (ODEs) [14, 15], written in the synodic reference frame:

$$\begin{aligned} \frac{d\boldsymbol{\rho}}{dt} &= \boldsymbol{\mathcal{V}} \\ \frac{d\boldsymbol{\mathcal{V}}}{dt} &= \boldsymbol{g}(\boldsymbol{\rho}) + \boldsymbol{h}(\boldsymbol{\mathcal{V}}) + \frac{\boldsymbol{T}}{m} \\ \frac{dm}{dt} &= -\frac{T}{c} \end{aligned} \tag{1}$$

where $\boldsymbol{\rho} = \{\xi,\ \eta,\ \zeta\}^T$ and $\boldsymbol{\mathcal{V}} = \{\dot{\xi},\ \dot{\eta},\ \dot{\zeta}\}^T$ are the spacecraft position and velocity vectors, m is the spacecraft mass, $\boldsymbol{T} = \{T_\xi,\ T_\eta,\ T_\zeta\}^T$ is the thrust vector and $c = I_{sp}g_0$ is the effective exhaust velocity. The $\boldsymbol{g}(\boldsymbol{\rho})$ and $\boldsymbol{h}(\boldsymbol{\mathcal{V}})$ functions, introduced to compact the set of ODEs, are defined as

$$\boldsymbol{g}(\boldsymbol{\rho}) = \begin{Bmatrix} \xi - \frac{1-\mu}{\rho_{13}^3}(\xi+\mu) - \frac{\mu}{\rho_{23}^3}[\xi-(1-\mu)] \\ \eta - \frac{1-\mu}{\rho_{13}^3}\eta - \frac{\mu}{\rho_{23}^3}\eta \\ -\frac{1-\mu}{\rho_{13}^3}\zeta - \frac{\mu}{\rho_{23}^3}\zeta \end{Bmatrix},$$

$$\boldsymbol{h}(\boldsymbol{\mathcal{V}}) = \begin{Bmatrix} 2\dot{\eta} \\ -2\dot{\xi} \\ 0 \end{Bmatrix}. \tag{2}$$

Table 1. *Physical constants*

Quantity	Unit	Value
Mass parameter μ	-	0.012150587
Distance unit	km	384400
Time unit	day	4.342479846

2.2 Near-Rectilinear Halo Orbit Computation

CR3BP dynamics is described by a time-invariant, autonomous system of epoch-independent equations that can be linearized to facilitate differential correction procedure, making it a very effective framework for generation of periodic orbits. Through the implementation of a single-shooting method and the utilization of the State Transition Matrix (STM), the differential correction process enables the identification and construction of exact periodic motions across specific families of orbits [16].

The orbit chosen as the reference one for the de-orbiting trajectories to be optimized is the NRHO selected by NASA for the LOP-G, depicted in Fig. 1.

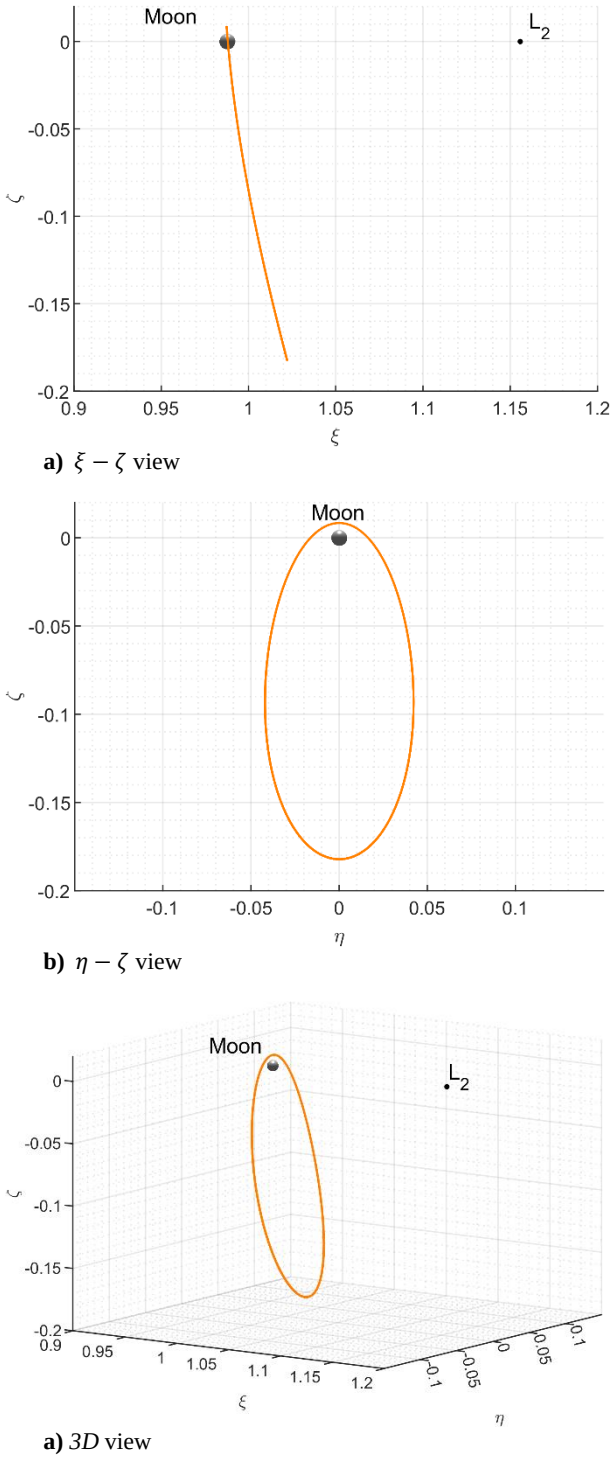

a) $\xi - \zeta$ view

b) $\eta - \zeta$ view

a) *3D* view

Figure 1*: Southern 9:2 synodic resonant EML₂ NRHO*

This specific orbit belongs to the southern family of the EML_2 NRHOs and presents a 9:2 lunar synodic resonance, indicating that the spacecraft completes 9

Copyright ©2024 by the International Astronautical Federation (IAF). All rights reserved.

revolutions along its periodic orbit per 2 synodic cycles of the Moon.

2.3 OCT in CR3BP trajectory optimization

The objective of OCT is to determine a control signal that will cause a process to satisfy the physical constraints and at the same time minimize (or maximize) a merit index $\mathcal{J}$ [17]. Its application to the specific optimization problem of this study aims at finding the optimal control law, specifically the thrust vector $\boldsymbol{T}$, that maximize the final mass of the spacecraft at the end of the trajectory. Hence, according to Mayer's formulation of the problem, the merit index to be maximized coincides with the spacecraft's final mass

$$\mathcal{J} = m_f \,. \tag{3}$$

The state vector $\boldsymbol{x}$ and its evolution over time $\dot{\boldsymbol{x}}$ have the form of

$$\begin{aligned} \boldsymbol{x} &= \left\{\xi, \eta, \zeta, \dot{\xi}, \dot{\eta}, \dot{\zeta}, m\right\}^T, \\ \dot{\boldsymbol{x}} &= \boldsymbol{f}(\boldsymbol{x}(t), \boldsymbol{T}(t), t) \,, \end{aligned} \tag{4}$$

with specific boundary conditions that might include constraints on the state variables at the external boundaries and, eventually, time constraints, expressed as a set of algebraic equations

$$\boldsymbol{\chi}\left(\boldsymbol{x}_0, \boldsymbol{x}_f, t_0, t_f\right) = \boldsymbol{0} \,. \tag{5}$$

A fundamental aspect of the employed indirect method is the transformation of the original TPBVP into an augmented version with new potential unknowns but with the ability to impose conditions that ensure the optimality of the solution, thus resolving the problem "indirectly". By introducing the so-called adjoint vector

$$\boldsymbol{\lambda} = \left\{\lambda_\xi,\ \lambda_\eta,\ \lambda_\zeta,\ \lambda_{\dot{\xi}},\ \lambda_{\dot{\eta}},\ \lambda_{\dot{\zeta}},\ \lambda_m\right\}^T, \tag{6}$$

one obtains the augmented state vector of the problem:

$$\bar{\boldsymbol{x}} = \{\boldsymbol{x}^T,\ \boldsymbol{\lambda}^T\}^T \,. \tag{7}$$

The derivation of the optimality condition begins by defining an augmented merit index, $\bar{\mathcal{J}}$, which incorporates a measure of the adherence to constraints and state quantities in relation to the ODEs governing the dynamical model. Let $\boldsymbol{\nu}$ be a vector containing the Lagrange multipliers, related to the boundary conditions. Hence $\bar{\mathcal{J}}$ is defined as

$$\bar{\mathcal{J}} = \mathcal{J} + \boldsymbol{\nu}^T \boldsymbol{\chi} + \int_{t_0}^{t_f} [\boldsymbol{\lambda}^T (\boldsymbol{f} - \dot{\boldsymbol{x}})]\, dt \,. \tag{8}$$

It is apparent that when both the boundary conditions and the equations of motion are fulfilled, there's a direct equivalence between solving the problem with the functional $\mathcal{J}$ or with its augmented counterpart $\bar{\mathcal{J}}$.

At this point it is worth defining the Hamiltonian

$$\begin{aligned} \mathcal{H} &= \boldsymbol{\lambda}^T \boldsymbol{f} = \\ &= \boldsymbol{\lambda}_\rho^T \boldsymbol{\mathcal{V}} + \boldsymbol{\lambda}_{\mathcal{V}}^T \left[\boldsymbol{g}(\boldsymbol{\rho}) + \boldsymbol{h}(\boldsymbol{\mathcal{V}}) + \frac{\boldsymbol{T}}{m}\right] - \lambda_m \frac{T}{c} \end{aligned} \tag{9}$$

where $\boldsymbol{\lambda}_\rho = \left\{\lambda_\xi,\ \lambda_\eta,\ \lambda_\zeta\right\}^T$, while the vector $\boldsymbol{\lambda}_{\mathcal{V}} = \left\{\lambda_{\dot{\xi}},\ \lambda_{\dot{\eta}},\ \lambda_{\dot{\zeta}}\right\}^T$ is called primer vector.

The fundamental condition that guarantees the solution's optimality is the stationarity of $\bar{\mathcal{J}}$. In other words, at the optimal solution, the augmented merit index reaches a stationary value, indicating that a local extremum (either a minimum or a maximum, depending on the problem formulation) has been achieved. From this, different sets of conditions arise. The transversality and optimality conditions enable the definition of new constraints on the augmented problem involving states, costates and Hamiltonian at initial and final times:

$$\frac{\partial \mathcal{J}}{\partial t_0} + \boldsymbol{\nu}^T \frac{\partial \boldsymbol{\chi}}{\partial t_0} - \mathcal{H}_0 = 0 \,, \tag{10a}$$

$$\frac{\partial \mathcal{J}}{\partial t_f} + \boldsymbol{\nu}^T \frac{\partial \boldsymbol{\chi}}{\partial t_f} + \mathcal{H}_f = 0 \,, \tag{10b}$$

$$\frac{\partial \mathcal{J}}{\partial \boldsymbol{x}_0} + \boldsymbol{\nu}^T \frac{\partial \boldsymbol{\chi}}{\partial \boldsymbol{x}_0} + \boldsymbol{\lambda}_0^T = \boldsymbol{0} \,, \tag{10c}$$

$$\frac{\partial \mathcal{J}}{\partial \boldsymbol{x}_f} + \boldsymbol{\nu}^T \frac{\partial \boldsymbol{\chi}}{\partial \boldsymbol{x}_f} - \boldsymbol{\lambda}_f^T = \boldsymbol{0} \,. \tag{10d}$$

The temporal evolution of the adjoint variables is determined by the Euler-Lagrange equations (their explicit form is presented in Appendix A.1)

$$\frac{d\boldsymbol{\lambda}}{dt} = -\left(\frac{\partial \mathcal{H}}{\partial \boldsymbol{x}}\right)^T \,, \tag{11}$$

while the algebraic equations for the controls determine the behaviour of controls over time:

$$\left(\frac{\partial \mathcal{H}}{\partial \boldsymbol{T}}\right)^T = 0 \,. \tag{12}$$

As in the case of the thrust of a propulsion system, elements of control vector can be subject to constraints. When explicit admissibility constraints are involved, the Eq. (12) might not yield the optimal controls. Searching for a solution that necessitates a control beyond these constraints would be impractical. At this point it is useful to introduce the Pontryagin's Maximum Principle [18], which states that the optimal control value in any point of the trajectory is the one that belongs to the admissibility domain and maximize the Hamiltonian in that point. By collecting all terms in Eq. (9) that multiply the thrust into the switching function $\mathcal{S}_F$, yields

$$\mathcal{H} = \boldsymbol{\lambda}_\rho^T \boldsymbol{\mathcal{V}} + \boldsymbol{\lambda}_{\mathcal{V}}^T [\boldsymbol{g}(\boldsymbol{\rho}) + \boldsymbol{h}(\boldsymbol{\mathcal{V}})] + T\, \mathcal{S}_F \,, \tag{13}$$

in which

Copyright ©2024 by the International Astronautical Federation (IAF). All rights reserved.

$$S_F = \frac{\boldsymbol{\lambda}_V^T \boldsymbol{T}}{m} \frac{}{T} - \frac{\lambda_m}{c} . \tag{14}$$

Being the control vector composed by the thrust vector $\boldsymbol{T}$ (defined by magnitude and direction), it turns out that $\mathcal{H}$ is linear with respect to the control itself. Therefore, the necessity of a bang-bang control arises [16]:

- $T = 0$ if $S_F \leq 0$. This means that $\mathcal{H}$ is maximized if the control is set to its minimum admissible value.
- $T = T_{max}$ if $S_F > 0$. Giving the control its maximum admissible value, the maximization of $\mathcal{H}$ is ensured.

In the synodic RF the trust vector can be expressed in synodic components by means of two angles, α and β, shown in the Figure 2.

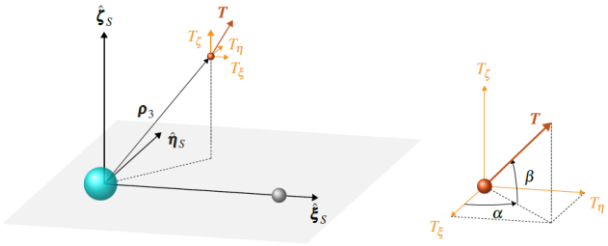

***Figure 2**: Thrust angles and components in the synodic RF*

Hence,

$$\boldsymbol{T} = \begin{Bmatrix} T_\xi \\ T_\eta \\ T_\zeta \end{Bmatrix} = T \begin{Bmatrix} \cos\beta \cos\alpha \\ \cos\beta \sin\alpha \\ \sin\beta \end{Bmatrix} . \tag{15}$$

From Lawden's work, the optimal thrust direction is parallel to the primer vector [19]. Therefore

$$\begin{aligned} \cos\beta \cos\alpha &= \frac{\lambda_\xi}{\lambda_V} \\ \cos\beta \sin\alpha &= \frac{\lambda_\eta}{\lambda_V} \\ \sin\beta &= \frac{\lambda_\zeta}{\lambda_V} , \end{aligned} \tag{16}$$

where $\lambda_V = \|\boldsymbol{\lambda}_V\|$.

All the tools are available to solve the TPBVP introduced so far, governed by the set of ODEs (1) to be integrated iteratively in order to find the optimal initial state $\bar{\boldsymbol{x}}_0^*$ which allows the trajectory to lead to the desired final state while respecting the imposed constraints. The key to the implemented single-shooting method lies in the adjustment of the initial conditions based on the discrepancies observed at the final boundary, via differential correction [16]. This adjustment process involves the use of iterative techniques which refines the initial conditions at each r-th step by means of the Jacobian matrix. The first iteration is started by integrating the set of equations with a guess initial vector $\boldsymbol{q}_r = \bar{\boldsymbol{x}}_0$ and computing the error on BCs. With a first order Taylor expansion, one can express the error on BCs at the (r+1)-th iteration as a function of the error on BCs and the state vector at the previous r-th one, and then retrieve the new initial state searching for $\boldsymbol{\chi}(\boldsymbol{q}_{r+1}) = \boldsymbol{0}$:

$$\boldsymbol{\chi}(\boldsymbol{q}_{r+1}) = \boldsymbol{\chi}(\boldsymbol{q}_r) + \left[\frac{\partial \boldsymbol{\chi}(\boldsymbol{q}_r)}{\partial \boldsymbol{q}_{r+1}}\right] (\boldsymbol{q}_{r+1} - \boldsymbol{q}_r) , \tag{17}$$

$$\boldsymbol{q}_{r+1} = \boldsymbol{q}_r - \left[\frac{\partial \boldsymbol{\chi}(\boldsymbol{q}_r)}{\partial \boldsymbol{q}_{r+1}}\right]^{-1} \boldsymbol{\chi}(\boldsymbol{q}_r) . \tag{18}$$

The term containing the partial derivatives represents the Jacobian matrix $\boldsymbol{G}(\boldsymbol{\chi}_r, \boldsymbol{q}_{r+1})$, which provides both quantitative and qualitative insights into how small changes in $\boldsymbol{q}_r$ impact on the problem. Its computation is approximated by means of forward finite-differences method, making the code much faster and more versatile for analysis with different constraints and BCs. Pursuing this direction, ODEs integration is performed in Python environment via the LSODA function pre-compiled in C++ [20], implementing an implicit multistep numerical method based on the Adams-Moulton formulations with variable step size and order [21]. Using a Python integrator precompiled in C++ offers significant advantages such as improved performance and computational efficiency, due to C++'s faster execution for intensive numerical operations due to machine-level compilation, while still maintaining Python's highly flexible and simple working environment.

The Jacobian computation within the iterative differential correction process may introduce inaccuracies that potentially threaten the method's convergence, leading to divergences. To refine the process certain strategies are incorporated. One such strategy is the application of a relaxation factor during the update step of the iterative process:

$$\boldsymbol{q}_{r+1} = \boldsymbol{q}_r - \kappa_1 \, [\boldsymbol{G}(\boldsymbol{\chi}_r, \boldsymbol{q}_{r+1})]^{-1} \, \boldsymbol{\chi}_r , \tag{19}$$

where appropriate values of $\kappa_1 = 1\times10^{-3} \div 1\times10^{-5}$ are beneficial to guarantee the convergence. In the initial stages of the iterative process, when the unknown values are being approximated with rough guesses, it is prudent to use lower values for κ_1. As the solution begins to approach the vicinity of the optimal value, higher values of can be employed depending on how sensitive the problem is. Another strategy involves the control on the subsequent error with respect to the error indicated by $\boldsymbol{\chi}$ at the previous step:

$$E_{max,r+1} < \kappa_2 \, E_{max,r} , \tag{19}$$

where $E_{max,i} = \max(\boldsymbol{\chi}_i)$, and a value of $\kappa_2 = 2 \div 3$ proves to be effective in supporting the initial phase of

Copyright ©2024 by the International Astronautical Federation (IAF). All rights reserved.

the iterative process. If the equation (19) is not satisfied, κ_1 is subject to a bisection method, which may be applied up to five iterations to refine the solution. This approach can encourage convergence despite a possible initial increase in the maximum error, as it helps to establish the appropriate direction towards optimality within the search space.

3. Boundary conditions

Having established the mathematical foundations of the problem, in order to fully define and solve it, it is necessary to provide the initial and terminal conditions of the problem.

The physical and propulsion characteristics of the spacecraft used in the analysis must be specified and are summarized in Table 1, essential for evaluating the propellant consumption. The reference values indicated for the thruster pertain to a Xenon Hall-effect currently undergoing testing [22].

Table 2. *Spacecraft characteristic values*

Quantity		Unit	Value
Initial mass	m_0	[kg]	600
Thrust	T	[T]	0.6
Specific Impulse	I_{sp}	[s]	2800

Once the optimal trajectory is determined, the final mass is obtained immediately, and consequently, the mass of consumed propellant can be calculated as

$$m_p = m_0 - m_f \,. \tag{19}$$

Subsequently, the ΔV required to deorbit the satellite can be derived using the Tsiolkovsky equation:

$$\Delta V = -I_{sp} g_0 \ln\left(\frac{m_f}{m_0}\right). \tag{20}$$

3.1 Terminal conditions

The final position target for the deorbiting trajectories is a designated graveyard region on the lunar surface at the lunar north pole identified by the synodic coordinates $\boldsymbol{\rho}_f = \{1-\mu,\ 0\ ,\ 4.519\times10^{-3}\}^T$. In terms of velocities, as this is an EOL disposal strategy, a soft landing is not considered. Therefore, the $\dot{\xi}$ and $\dot{\eta}$ velocities are not targeted; instead, a negative $\dot{\zeta} = -0.05$ is imposed to guide optimization towards trajectories reaching the north pole from above and not intersecting the Moon's body. As a consequence of transversality and optimality conditions, the adjoint variables λ_{ξ_f}, λ_{η_f}, λ_{ζ_f}, $\lambda_{\dot{\zeta}_f}$ and both $\mathcal{H}_0$ and $\mathcal{H}_f$ are free, $\lambda_{\dot{\xi}_f}$ and $\lambda_{\dot{\eta}_f}$ at the final time must be null (since the corresponding variables are free) while λ_{m_f} is set to 1, as m_f is the subject of maximization. In a concise form, the reduced set of terminal boundary conditions is

$$\boldsymbol{\chi}_f = \left\{\xi_f,\ \eta_f,\ \zeta_f,\ \dot{\zeta}_f,\ \lambda_{\dot{\xi}_f},\ \lambda_{\dot{\eta}_f},\ \lambda_{m_f},\ \tau_f\right\}^T$$
$$= \left\{0.988, 0, 4.519\times10^{-3}, -0.05, 0, 0, 1,\ \tau_f\right\}^T \tag{21}$$

Since in the implemented dynamic model the Hamiltonian is extremely sensitive to differential corrections, fixed-time analyses have been opted for, modifying τ_f for each analysis according to the starting point in order to accommodate mission times, spacing in a dimensional range of 5.475 days ÷ 9.740 days. Since a time constraint can lead to finding sub-optimal solutions (being optimal solutions for that specific time, but not in general), an attempt was made to perform a sensitivity analysis on time, by appropriately varying the final time of first convergence per each point and analyzing the behavior of $\mathcal{S}_F$ and consequently m_p.

The iterative procedure is stopped when the norm of the errors on the final boundary conditions reaches a certain tolerance. In this case, a tolerance of 1×10^{-7} has been set for errors on all BCs except for ξ_f and η_f, whose tolerance is increased to 1×10^{-4} by characterizing a region around the north pole.

3.2 Initial conditions

The analysis is conducted by optimizing various de-orbiting trajectories that originate from different points of the selected NRHO. The initial positions and velocities of the spacecraft have been calculated through the integration performed to identify the periodic motion of the orbit. Specifically, considering the reference starting point as the furthest from the Moon, i.e., the apolune, the preceding and subsequent points of the orbit are indicated in terms of the percentage of orbital period elapsed, with 0% corresponding to the apolune. Negative and positive values indicate positions before or after the apolune in the orbit, respectively. The analysis considers 28 starting points, ranging from -35% to 32.5%, equally distributed in time along the NRHO.

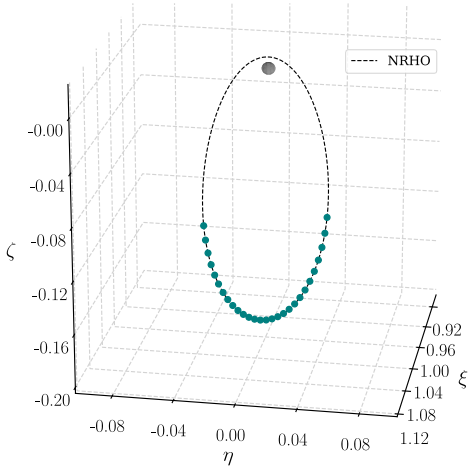

Figure 3*: Equal time distribution of starting point near apolune*

Copyright ©2024 by the International Astronautical Federation (IAF). All rights reserved.

The initial mass of the spacecraft is set to 600 kg, corresponding to 1 mass unit, while for each trajectory τ_0 is set to 0. Having thus assigned all positions, velocities, and the initial mass in the initial state vector, it follows that the initial guesses needed to start the iterative procedure refer to all the corresponding adjoint variables, encapsulated in the adjoint vector

$$\boldsymbol{\lambda}_0 = \{\lambda_{\xi_0},\ \lambda_{\eta_0},\ \lambda_{\zeta_0},\ \lambda_{\dot{\xi}_0},\ \lambda_{\dot{\eta}_0},\ \lambda_{\dot{\zeta}_0},\ \lambda_{m_0}\}^T. \quad (22)$$

To start the optimization procedure, reasonable initial guesses are essential. One of the disadvantages of indirect methods is that adjoint variables lack direct physical meaning, therefore their evolutions and influences could be more or less predictable. Consequently, inappropriate initial guesses for the adjoint variables can cause convergence problems due to the problem's high sensitivity to these values, making it crucial to provide well-considered initial values to ensure the optimization procedure converges effectively. For example, an interpretation of the velocity adjoint variables is linked to the importance of the primer vector, which dictates the optimal thrust direction. Indeed, the larger the adjoint in a velocity direction, the more thrust will be emphasized in that direction. If the adjoint is positive, the thrust will align with it; if negative, the thrust will oppose it. This interpretation highlights how the magnitude and sign of velocity adjoints guide the spacecraft's acceleration and deceleration to achieve the desired trajectory. Less intuitive, however, are the adjoints related to the synodic coordinates.

4. Fixed-time solutions

Based on the procedure outlined previously, the single shooting method via differential correction allowed for the computation of the various trajectories, each with its specific initial conditions, and proceeding through continuity. The first convergence of the iterative procedure led to the optimal de-orbiting trajectory starting from the apolune of the NRHO. As already noted, to limit the risk of encountering sub-optimal trajectories, the final time around the value of first convergence was varied delicately, thus analyzing its influence on the shape and position of the switching function. Figure 4 shows, for the first point analyzed, a lowering of $\mathcal{S}_F$ as τ_f increases. This results in a reduction of propellant consumption considering the shape of $\mathcal{S}_F$, which, when lowering, tends to enlarge the coasting arc. This type of investigation was conducted for each point chosen on the NRHO, where permitted by the numerical sensitivity of the problem.

Thus, based on the results obtained from the first point, an exploration was carried out on trajectories departing both before and after apolune position, resulting in the set of trajectories depicted in Figure 5a. It should be noted how the injection point for the transfer has a considerable impact on the disposal cost in terms of propellant, as indicated by the color map of m_p. For clarity, Figure 5b represents only the injection points on the NRHO, colored according to the propellant consumption of the associated trajectory.
Figure 6 shows the trend of the final time of each trajectory in days, demonstrating a natural decreasing trend as one progresses along the NRHO and starting from points that "facilitate" the trajectory for the disposal of the satellite into the desired area, not necessitating major directional deviations to reach the graveyard region.

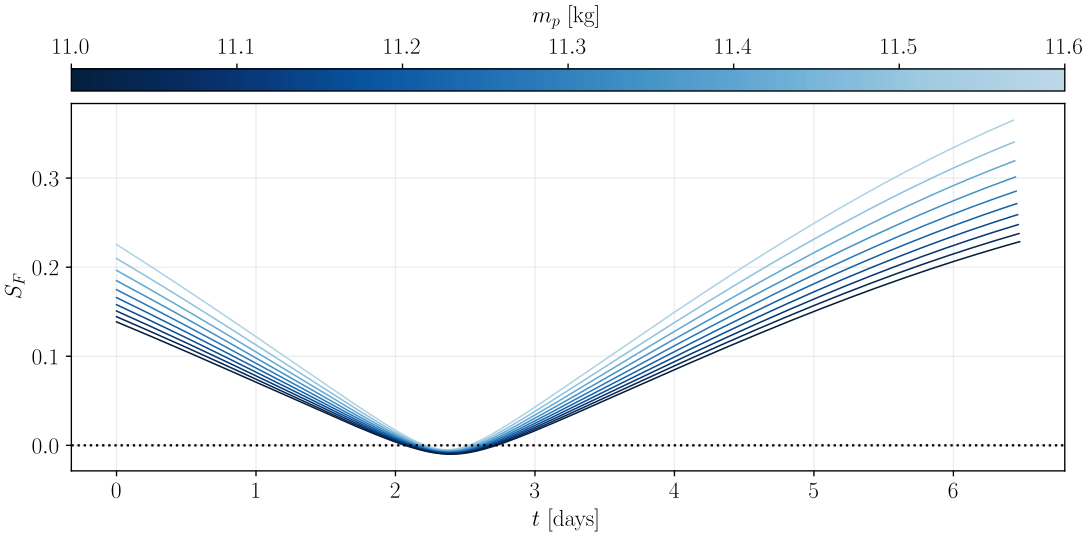

***Figure 4**: τ_f influence on $\mathcal{S}_F$*

Copyright ©2024 by the International Astronautical Federation (IAF). All rights reserved.

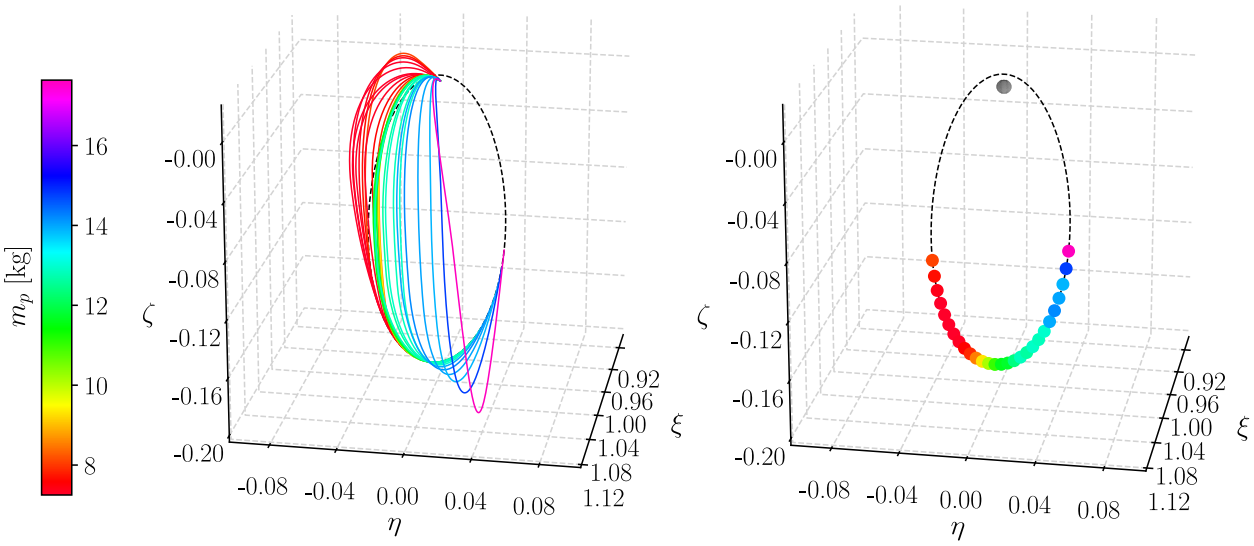

***Figure 5**: Optimal deorbiting trajectories*

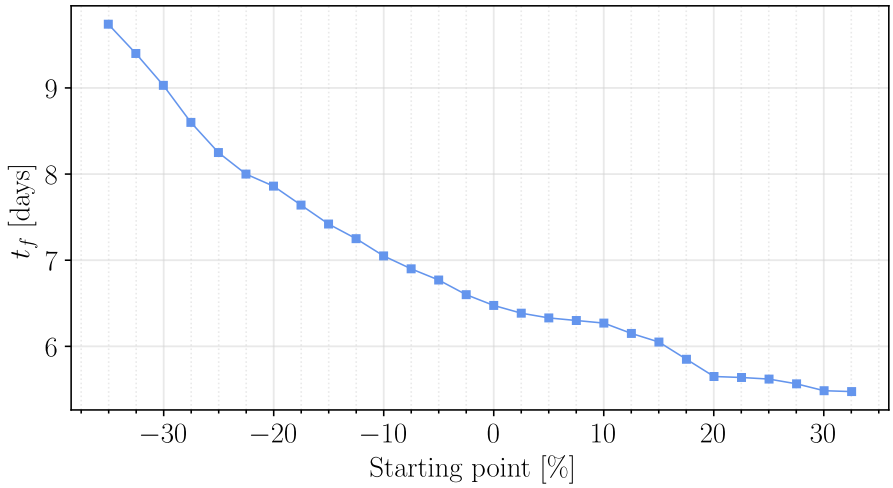

***Figure 6**: trend of final time in relation to injection point position*

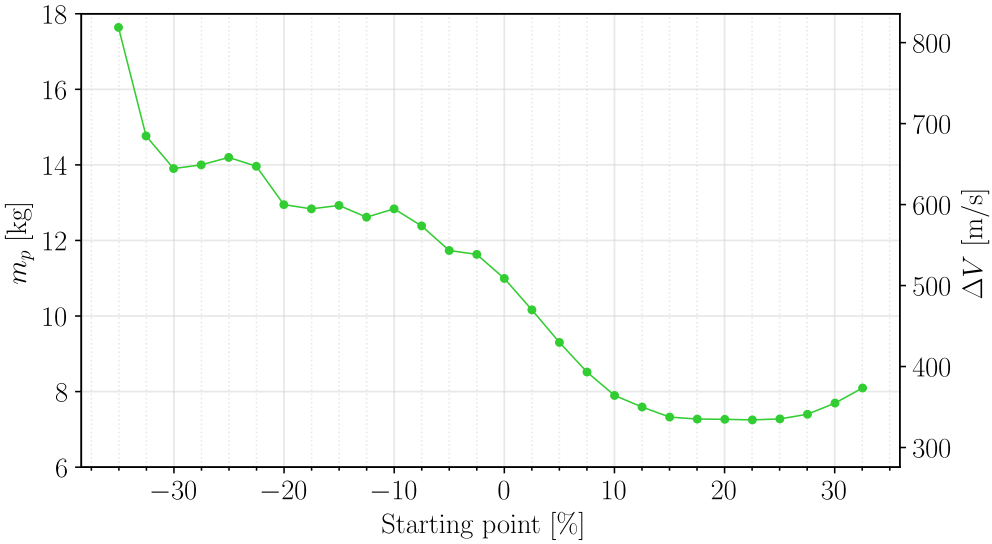

***Figure 7**: propellant consumption and required ΔV in relation to injection point position*

Copyright ©2024 by the International Astronautical Federation (IAF). All rights reserved.

Figure 7 presents the trend of propellant mass consumption and therefore required ΔV as a function of the injection point. Trajectories starting from points before the -35% of the orbit were not investigated due to their low interest given the increasing trend in consumption. Conversely, points beyond 32.5% of the orbit, given the satellite mass and thrust under consideration, do not allow for direct de-orbiting trajectories and thus cannot be compared with those previously determined. Of all the optimal de-orbiting trajectories obtained, those requiring the minimum propellant consumption (in nuances of red in Figs. 5a and 5b) depart from the portion of the orbit immediately following the apolune, clearly identifying a minimum near the point corresponding to 22.5% of the orbit, as can be seen in Figure 7.

The optimal minimum-propellant de-orbiting trajectory is depicted in Figure 8, where red and green colours indicate thrust and coasting arcs respectively. Its initial conditions and the value of $\boldsymbol{\lambda}_0^*$ that allows solving of TPBVP are summarized in Table 2.

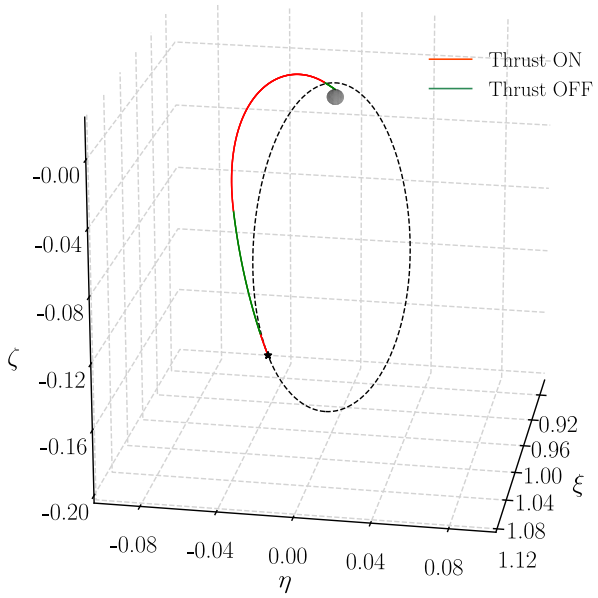

***Figure 8**: Minimum-propellant trajectory*

***Table 3**. Initial state and costate for the minimum-propellant solution*

Parameter	Value
$\boldsymbol{\rho}_0$	$\{1.014447, -0.032061, -0.152135\}^T$
$\boldsymbol{\mathcal{V}}_0$	$\{-0.044099, -0.074989, 0.181507\}^T$
m_0	1
$\boldsymbol{\lambda}_{\rho_0}^*$	$\{0.020814, 0.027155, 0.030372\}^T$
$\boldsymbol{\lambda}_{\mathcal{V}_0}^*$	$\{0.030307, 0.015413, -0.016221\}^T$
$\boldsymbol{\lambda}_{m_0}^*$	0.987661

The final time that showed the best results within the convergence limits of the code is $t_f = 5.6385$ days. Figure 9 shows the time evolution of each position and velocity component during such trajectory observing how the boundary conditions imposed on ξ, η, ζ and $\dot{\zeta}$ are met at t_f. Notice how slope variations correspond to specific moments in the trajectory when the thruster is activated or deactivated.

To interpret what happens from a dynamic perspective, it is useful to observe the trends of α and β, which are the angles in the $\hat{\boldsymbol{\xi}} - \hat{\boldsymbol{\eta}}$ plane and out of the plane (refer to Fig. 2) respectively. From Figure 10, it can be observed that α starts from a positive value of about 25° and increases monotonically. Initial values are indicative of a deviation from the dotted NRHO in the first red arc in which the thrust has a dominant braking effect on the negative $\dot{\xi}$, as outlined by the positive $\lambda_{\dot{\xi}_0}$ value, greater than the other adjoint velocity variables. Then, in the second thrust arc an increasingly predominant thrust in the positive $\hat{\boldsymbol{\eta}}$ and negative $\hat{\boldsymbol{\zeta}}$ directions is observed, which causes the trajectory to close to curve and reach the designated point. Indeed, as shown in Figure 12, β starts from a negative value of $-25°$ and decreases monotonically, indicating a braking action against the positive $\dot{\zeta}$, reaching values of $-80° \div -85°$ in the second thrust arc, contributing to the curvature of the trajectory and its subsequent closure towards the lunar north pole.

Figure 11 presents the switching function and mass profile for the entire minimum-propellant trajectory. The bang-bang control, derived from Pontryagin's Maximum Principle, dictates that the thrust is activated whenever $\mathcal{S}_F$ is positive, thus defining the thrust arcs of the trajectory. The percentage of time during which the switching function assumes negative values, effectively constituting the coasting phases, amounts to 32% of t_f. In such time intervals the mass of the spacecraft remains constant. On the contrary, during the the time intervals when the switching function is positive, depicted in red in Figure 8, there is a reduction in mass because propellant is being consumed. The final mass turns out to be $m_f = 592.7496$ kg, which corresponds to $m_p = 7.2504$ kg and $\Delta V = 333.5484$ m/s. This reduction in propellant required for de-orbiting of up to 60% allows the mission to allocate more fuel for earlier operational phases, effectively extending the mission's operational lifespan.

An interesting result is shown in Figure 12, which displays the behaviors of the different switching functions. These functions pertain to each optimal trajectory departing from points with relative positions to apolune in the range of 0% to 32.5%. For clarity, the ranges are divided into 0% to 20% and 20% to 32.5%.

Copyright ©2024 by the International Astronautical Federation (IAF). All rights reserved.

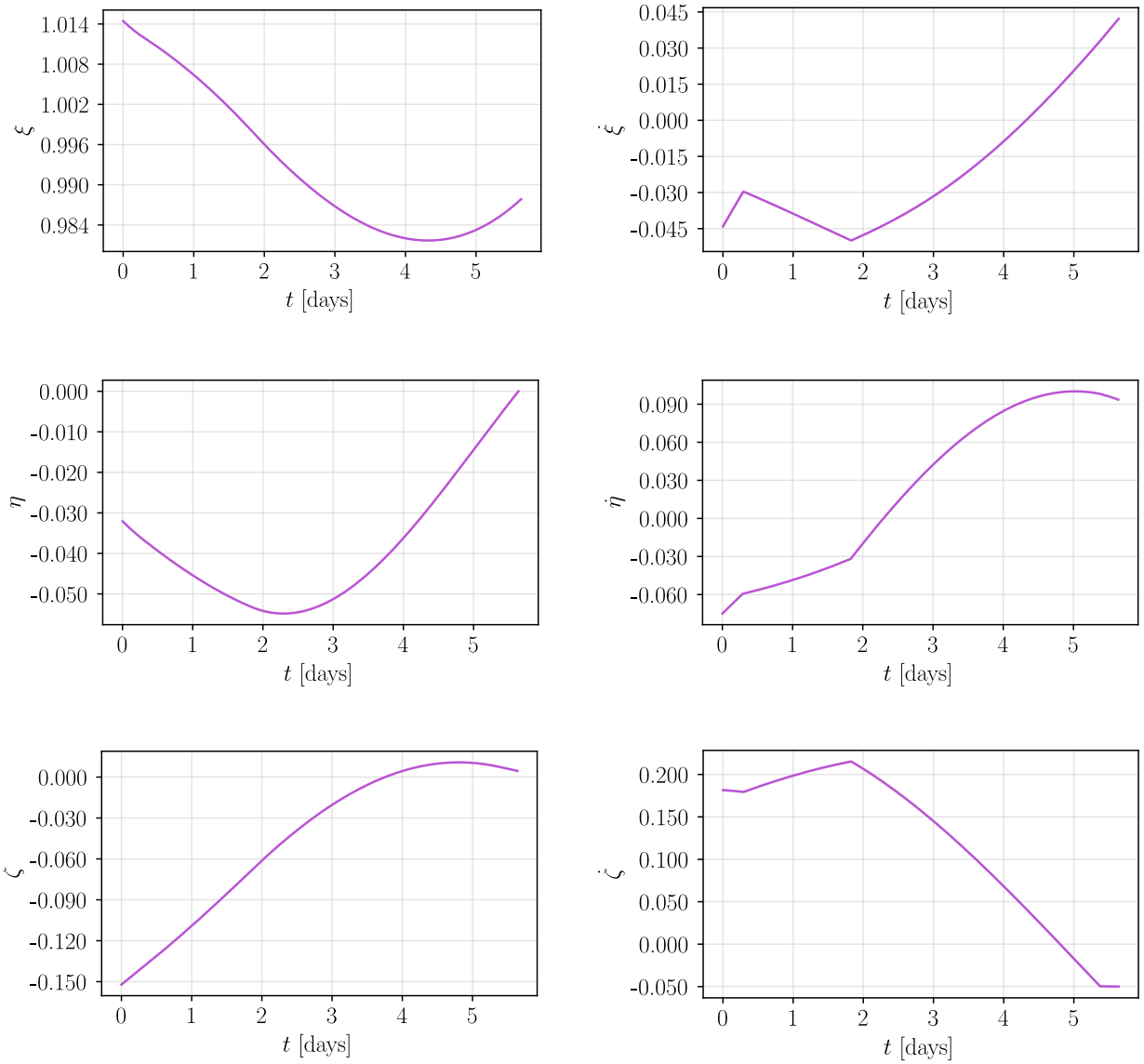

***Figure 9**: Evolution in time of synodic positions and velocities of the minimum-propellant trqjectory*

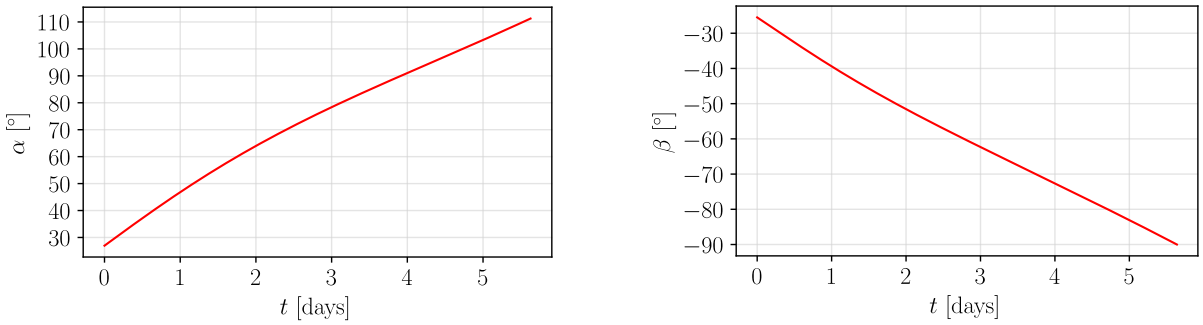

***Figure 10**: Evolution in time of thrust angles of the mininum-propellant trajectory*

Copyright ©2024 by the International Astronautical Federation (IAF). All rights reserved.

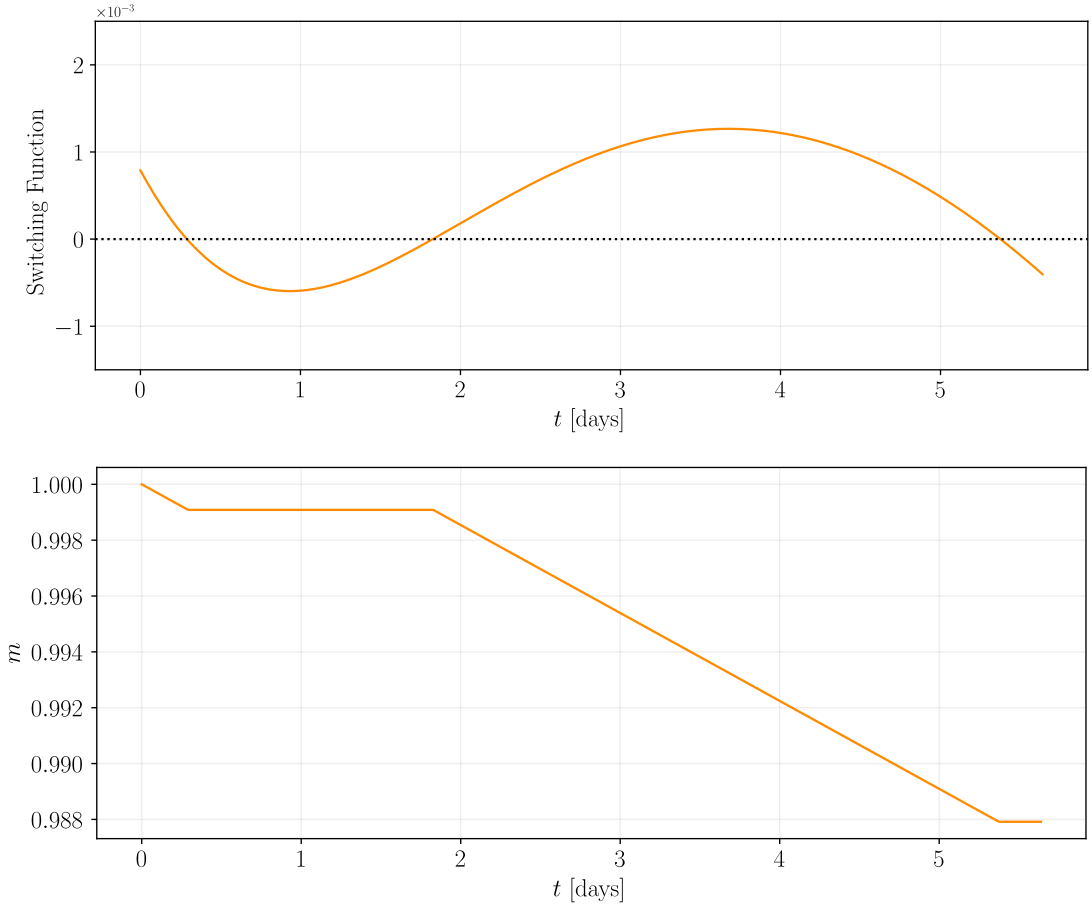

***Figure 11**: Evolution in time of switching function and mass of the minimum-propellant trajectory*

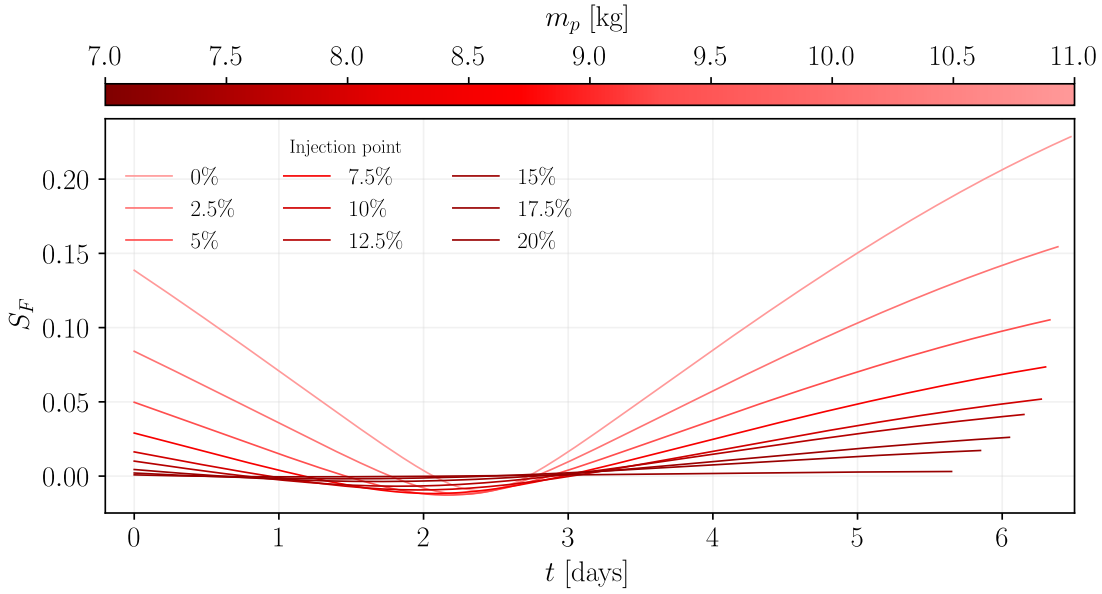

a) Focus on $\mathcal{S}_F$ of 0 % ÷ 20 % departing point trajectories

Copyright ©2024 by the International Astronautical Federation (IAF). All rights reserved.

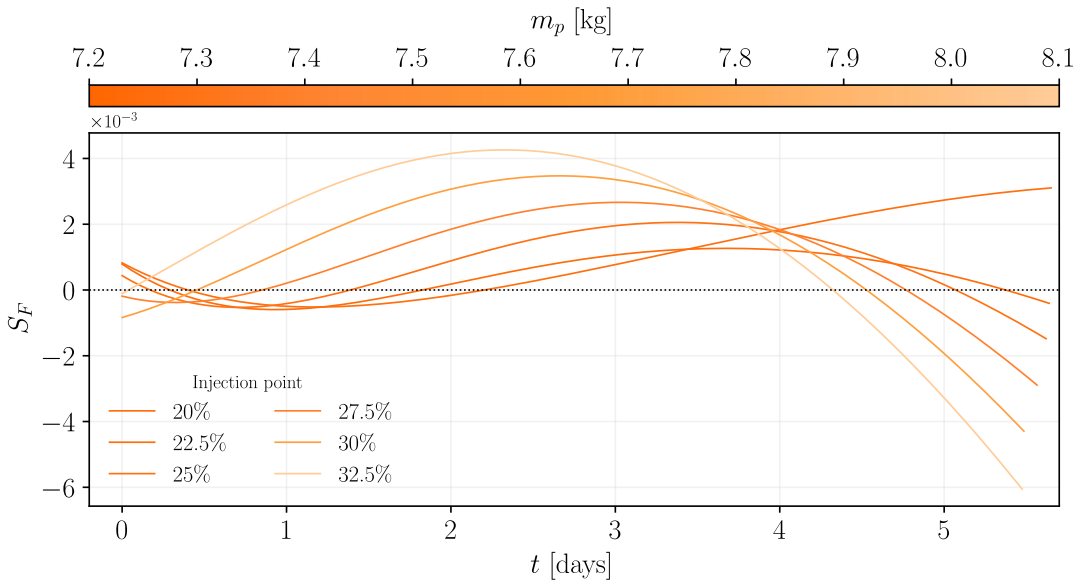

b) Focus on $\mathcal{S}_F$ of 20 % ÷ 32.5 % departing point trajectories

***Figure 12**: Behavior of $\mathcal{S}_F$ under different analysis conditions*

These intervals correspond to the orbital arc that demonstrates clear advantages in terms of propellant burned (refer to Fig. 7). Figure 12a focuses on the first range, corresponding to the descending phase of the m_p trend. The switching functions belong to the same family (thrust-coast-thrust, or T-C-T phases) but tend to decrease their slope at the initial and final segments, flattening along the zero ordinate as the injection point progresses along the NRHO. Consequently, this tends to extend the coasting phase, thereby progressively reducing the m_p. In Figure 13b, a transition is observed from switching functions of the T-C-T type to T-C-T-C (like the minimum consumption one shown in Fig. 8) and C-T-C types, with a slight increasing trend in m_p, due to longer durations of thrust arcs. Indeed, the switching functions tend to bulge towards positive values, activating the thrust for a longer duration.

5. Conclusions

The choice of this scenario aligns with the growing interest in cislunar space in recent years, as evidenced by the increasing number of space missions focusing on periodic and quasi-periodic orbits around the Earth-Moon Lagrangian points. Additionally, with the advancement of the Artemis program, these specific orbits may become prime staging areas for efforts to colonize the Moon and the near-Earth space. The chosen representative orbit for this case study is the Near-Rectilinear Halo Orbit where the construction of the Lunar Orbital Platform-Gateway is planned. Within the CR3BP framework, its periodic motion around L_2 has been computed by means of single shooting and differential correction strategies.

The NASA-led ambitious program, along with many other planned space missions, will increasingly attract stakeholder interest in cislunar space. Consequently, there will be a growing need to implement appropriate end-of-life strategies to reduce space debris. This proactive approach is essential for ensuring sustainable and safe operations in the cislunar environment, as the number of missions and activities in this region is expected to rise significantly. As a result, it has become interesting to explore a direct disposal strategy involving the deorbiting of a satellite into a designated graveyard region near the lunar north pole.

As the central core of this study, the problem has been formulated as an optimal control problem. The optimization was carried out using an indirect approach based on Optimal Control Theory, that transformed the optimal control problem into a two-point boundary value problem, solved employing a single-shooting method via differential correction. Different initial conditions on the NRHO were considered, conducting a parametric study of the propellant mass consumed relative to the injection point. Necessary and optimality conditions were derived, and the bang-bang control was defined in accordance with the Pontryagin's Maximum Principle. The implemented indirect method has proven to be very precise and suitable for complex optimization problems with dynamics that are far from simple and straightforward. Despite typical numerical issues of non-convergence, these were mitigated by specific strategies aimed at strengthening the code.

Copyright ©2024 by the International Astronautical Federation (IAF). All rights reserved.

Appendix A

A.1 Euler-Lagrange equations

$$\dot{\lambda}_\xi = -\lambda_\xi \left[1 - \frac{1-\mu}{\rho_{13}^3} + \frac{3(1-\mu)(\xi+\mu)^2}{\rho_{13}^5} + - \frac{\mu}{\rho_{23}^3} + \frac{3\mu(\xi-1+\mu)^2}{\rho_{23}^5}\right] + -\lambda_\eta \left[\frac{3(1-\mu)(\xi+\mu)\eta}{\rho_{13}^5} + \frac{3\mu(\xi-1+\mu)\eta}{\rho_{23}^5}\right] + -\lambda_\zeta \left[\frac{3(1-\mu)(\xi+\mu)\zeta}{\rho_{13}^5} + \frac{3\mu(\xi-1+\mu)\zeta}{\rho_{23}^5}\right] \quad (23)$$

$$\dot{\lambda}_\eta = -\lambda_\xi \left[\frac{3(1-\mu)(\xi+\mu)\eta}{\rho_{13}^5} + \frac{3\mu(\xi-1+\mu)\eta}{\rho_{23}^5}\right] + -\lambda_\eta \left[1 - \frac{1-\mu}{\rho_{13}^3} + \frac{3(1-\mu)\eta^2}{\rho_{13}^5} - \frac{\mu}{\rho_{23}^3} + \frac{3\mu\eta^2}{\rho_{23}^5}\right] + -\lambda_\zeta \left[\frac{3(1-\mu)\eta\zeta}{\rho_{13}^5} + \frac{3\mu\eta\zeta}{\rho_{23}^5}\right] \quad (24)$$

$$\dot{\lambda}_\zeta = -\lambda_\xi \left[\frac{3(1-\mu)(\xi+\mu)\zeta}{\rho_{13}^5} + \frac{3\mu(\xi-1+\mu)\zeta}{\rho_{23}^5}\right] + -\lambda_\eta \left[\frac{3(1-\mu)\eta\zeta}{\rho_{13}^5} + \frac{3\mu\eta\zeta}{\rho_{23}^5}\right] + -\lambda_\zeta \left[-\frac{1-\mu}{\rho_{13}^3} + \frac{3(1-\mu)\zeta^2}{\rho_{13}^5} - \frac{\mu}{\rho_{23}^3} + \frac{3\mu\zeta^2}{\rho_{23}^5}\right] \quad (25)$$

$$\dot{\lambda}_\dot{\xi} = -\lambda_\xi - 2\lambda_\dot{\eta} \quad (26)$$

$$\dot{\lambda}_\dot{\eta} = -\lambda_\eta + 2\lambda_\dot{\xi} \quad (27)$$

$$\dot{\lambda}_\dot{\zeta} = -\lambda_\zeta \quad (28)$$

$$\dot{\lambda}_m = \frac{T}{m^2}\lambda_v \quad (29)$$

References

[1] P. Giordano, et al. "Moonlight navigation service-how to land on peaks of eternal light." *Proceedings of the 72nd International Astronautical Congress (IAC), Dubai, United Arab Emirates*. 2021.

[2] M. Woodard, D. Folta, and D. Woodfork. "ARTEMIS: the first mission to the lunar libration orbits." *21st International Symposium on Space Flight Dynamics, Toulouse, France*. 2009.

[3] National Aeronautics and Space Administration. ARTEMIS (THEMIS). 2007, https://science.nasa.gov/mission/themis-artemis/, (accessed 12.12.23).

[4] X. Yingzhuo. "China's planning for deep space exploration and lunar exploration before 2030." *Space Sci* 38.5 (2018): 591-592.

[5] K. Oshima, et al. "EQUULEUS mission analysis: design of the transfer phase." *International Symposium on Space Technology and Science, ISTS-2017-d-159, Ehime, Japan*. 2017.

[6] National Aeronautics and Space Administration. Artemis. 2007, https://www.nasa.gov/humans-in-space/artemis/, (accessed 04.11.23).

[7] National Aeronautics and Space Administration. "NASA's Lunar Exploration Program Overview". 2020.

[8] P. Guardabasso, S. Lizy-Destrez, and M. Ansart. "Lunar orbital debris mitigation: Characterisation of the environment and identification of disposal strategies". In *8th European Conference on Space Debris*, volume 8, 2021.

[9] P. Guardabasso, D. Skoulidou, L. Bucci, F. Letizia, and S. Lizy-Destrez. "Cislunar Debris Mitigation: Development of a Methodology to Assess the Sustainability of Lunar Missions". In *72nd International Astronautical Congress (IAC)*, 2021.

[10] M. Accettura. "Debris Mitigation and Atmospheric Deorbiting Analysis for Lunar L2 NRHO Departing Spacecraft". Diss. Politecnico di Torino, 2023.

[11] D. Andrievskaia, I. Cáceres, P. Guardabasso, S. Lizy-Destrez. "Analysis of Lunar Impacts for Orbital Debris Mitigation". In *73rd International Astronautical Congress (IAC), 2022.*

[12] National Aeronautics and Space Administration. Gravity Recovery and Interior Laboratory (GRAIL). https://science.nasa.gov/mission/grail/, 2011, (accessed 28.11.23).

[13] National Aeronautics and Space Administration. Lunar Atmosphere and Dust Environment Explorer (LADEE). https://science.nasa.gov/mission/ladee/, 2013, (accessed 28.11.23).

[14] C. Zhang, et al. "Low-thrust minimum-fuel optimization in the circular restricted three-body problem." *Journal of Guidance, Control, and Dynamics* 38.8 (2015): 1501-1510.

[15] K. Oshima, S. Campagnola, and T. Yanao. "Global search for low-thrust transfers to the Moon in the planar circular restricted three-body problem." *Celestial Mechanics and Dynamical Astronomy* 128 (2017): 303-322.

[16] L. Mascolo. "Low-Thrust Optimal Escape Trajectories from Lagrangian Points and Quasi-

Copyright ©2024 by the International Astronautical Federation (IAF). All rights reserved.

Periodic Orbits in a High-Fidelity Model". PhD thesis, Politecnico di Torino, 2023.

[17] D.E. Kirk. "Optimal control theory: an introduction". Courier Corporation, 2004.

[18] L.S. Pontryagin, V.G. Boltyanskii, R.V. Gamkrelidze, and E.F. Mishchenko. "The mathematical theory of optimal processes". *Interscience*, NY, 1962.

[19] D.F. Lawden. "Optimal Trajectories for Space Navigation". *Butterworths mathematical texts*. Butterworths, 1963.

[20] Lsoda - scipy v1.10.1 manual. https://docs.scipy.org/doc/scipy/reference/generated/scipy.integrate.LSODA.html.

[21] L. F. Shampine. "Computer solution of ordinary differential equations". *The initial value problem*, 1975.

[22] Aerojet Rocketdyne. Advanced Electric Propulsion System (AEPS). 2023, https://www.rocket.com/sites/default/files/documents/AEPS.pdf, (accessed 20.03.2024).